

## Article

# Investigation of the Inverse Magnus Effect on a Rotating Sphere in Hypersonic Rarefied Flow

Yazhong Jiang <sup>1,\*</sup> , Yuxing Ling <sup>2</sup> and Shikang Zhang <sup>3</sup>

<sup>1</sup> Hubei Key Laboratory of Theory and Application of Advanced Materials Mechanics, School of Science, Wuhan University of Technology, Wuhan 430070, China

<sup>2</sup> School of Science, Wuhan University of Technology, Wuhan 430070, China; 327364@whut.edu.cn

<sup>3</sup> School of Mechanical and Electronic Engineering, Wuhan University of Technology, Wuhan 430070, China; 327568@whut.edu.cn

\* Correspondence: jiangyazhong@whut.edu.cn

**Abstract:** Explorations involving long-endurance and maneuvering flights in the upper atmosphere, as well as research on atmospheric entries of space debris or asteroids, call for a full understanding of hypersonic rarefied flows. The inverse Magnus effect occurs in the hypersonic rarefied flow past a rotating sphere, but the aerodynamic behavior is contrary to the Magnus effect in the continuum flow regime. In this article, a series of such flows are numerically studied using the direct simulation Monte Carlo (DSMC) method. By analyzing the flow fields, as well as the distributions of pressure and shear stress on the sphere, the formation of the inverse Magnus force can be attributed to the tangential momentum transfer between incident gas molecules and the windward surface. The variation laws of aerodynamic parameters with the rotation rate are presented and discussed.

**Keywords:** hypersonic; rarefied gas effect; Magnus effect; DSMC method; upper atmosphere



**Citation:** Jiang, Y.; Ling, Y.; Zhang, S. Investigation of the Inverse Magnus Effect on a Rotating Sphere in Hypersonic Rarefied Flow. *Appl. Sci.* **2024**, *14*, 1042. <https://doi.org/10.3390/app14031042>

Academic Editor: Roberto Camussi

Received: 30 December 2023

Revised: 21 January 2024

Accepted: 23 January 2024

Published: 25 January 2024



**Copyright:** © 2024 by the authors. Licensee MDPI, Basel, Switzerland. This article is an open access article distributed under the terms and conditions of the Creative Commons Attribution (CC BY) license (<https://creativecommons.org/licenses/by/4.0/>).

## 1. Introduction

Hypersonic technology has been attracting wide attention for decades. As the scientific foundation of hypersonic flight, hypersonic aerodynamics has become a hotspot in the research on fluid mechanics and aerospace engineering. Many advances have been made to fully understand the various phenomena involved in hypersonic flows, such as thermochemical nonequilibrium processes under high-enthalpy conditions [1], hypersonic boundary-layer transition [2–4], and hypersonic propulsion [5]. Among these research areas, hypersonic rarefied flow [6,7] is academically challenging and also significant for engineering applications. Hypersonic rarefied flow has features that are shared by all hypersonic flows, and additionally, it is characterized by gas rarefaction due to the high altitude of flight. In rarefied gas flows, the translational motion of gas molecules can be highly nonequilibrium, leading to the breakdown of macroscopic governing equations for continuum gas flows. Knowledge based on continuum gas dynamics can be problematic for rarefied flows; thus, some phenomena found in rarefied flows are thought to be counter-intuitive [8].

In order to predict the trajectories of asteroids [9] and space debris [7,10], it is important to simulate hypersonic flow fields and compute the aerodynamic characteristics at high altitudes. For the highly rarefied flows over asteroids or space debris at the early stage of their atmospheric entries, gas-kinetic-based numerical methods [11] and experiments in low-density wind tunnels [10] are very useful research tools. In these investigations [7,9,10], the geometries of asteroids, space debris, or their fragments are usually treated as spheres. Along with their hypersonic velocities, these unmanned atmospheric-entry objects can also have remarkable spinning rates during their flights. In both continuum and rarefied flows, the rotation of a solid body can produce lift, thus changing its trajectory. It is worth noting that the aerodynamic laws governing rarefied flows over a rotating cylinder/sphere

are qualitatively different from the Magnus effect [12,13] observed in the continuum flow regime. This difference leads to theoretical and numerical investigations on the so called “inverse Magnus effect” [14,15] within the context of hypersonic rarefied flows.

Another motivation to study hypersonic rarefied flows and the inverse Magnus effect comes from the utilization of extremely low earth orbits and the upper atmosphere [16]. The altitude of the upper atmosphere ranges from 100 km to 200 km. Neither traditional orbiting spacecrafts nor emerging hypersonic vehicles can fulfil the requirements for long-endurance and maneuvering flight between 100 km and 200 km. To help fill this gap, it is crucial to further understand and make use of aerodynamic forces in the low-density atmosphere. Unfortunately, the lift-to-drag ratios ( $L/D$ ) of known aerodynamic configurations (e.g., waveriders) cannot meet the requirements for achieving both long endurance and maneuverability within this altitude interval (100 km–200 km). Shen et al. [16] pointed out that reducing the accommodation coefficient of the solid surface can elevate the  $L/D$  of the vehicle in the upper atmosphere. However, the accommodation coefficient needs to be as low as about 0.2 to achieve  $L/D > 1$ . Such a value of the accommodation coefficient is much lower than the existing data for surfaces made of common materials. In this paper, another potential approach to increase  $L/D$  in hypersonic rarefied flows will be explored, which relies on the inverse Magnus effect for rotating surfaces.

In the context of continuum aerodynamics, the Magnus effect in the flow over a rotating cylinder/sphere has been well studied [17]. Generally speaking, the rotation of the solid surface drives the ambient fluid to circulate because of the no-slip condition. As a consequence, the velocity distribution, and thus the pressure distribution, around the body become asymmetric. The pressure differences form a lift acting on the cylinder/sphere, which is also known as the Magnus force. Under normal conditions, the direction of the Magnus force  $F_M$  is the same as the direction of  $V_\infty \times \omega$  ( $V_\infty$  is the freestream velocity and  $\omega$  is the angular velocity of the rotating body). This Magnus effect in low-speed continuum flows is usually employed to explain the curved trajectory of a spinning ball in ball games [12]. In addition, it is also applied to ship propulsion [12], as well as high-lift devices for aircraft [13].

The inverse Magnus effect occurs under rarefied flow conditions; however, the direction of the lift is the same as  $\omega \times V_\infty$ , which is contrary to the Magnus force. This phenomenon cannot be explained by continuum flow theory. Indeed, the gas-kinetic theory and the related numerical methods must be used in order to understand the inverse Magnus effect. In the free-molecular regime, the theoretical formula for the inverse Magnus force was firstly obtained by Wang [18]. Then, Borg et al. [19] and Weidman et al. [14] extended Wang’s work from different points of view. The theories in [14,18,19] are consistent, but they are all limited to the free-molecular regime.

In the transition regime between continuum and free-molecular regimes, there is no analytical solution for the flow over a rotating cylinder/sphere. Hence, the study of the inverse Magnus effect must resort to numerical approaches. On the basis of the full Boltzmann equation, the direct simulation Monte Carlo (DSMC) method is the dominant and reliable simulation technique for hypersonic rarefied flows [20,21]. Recently, John et al. [15,22] carried out a systematic numerical investigation of hypersonic rarefied flows past a rotating cylinder, using two-dimensional (2D) DSMC simulations. In these works, the inverse Magnus force exerted on the cylinder was observed. Furthermore, the influences of different flow conditions on the inverse Magnus effect were studied. The influencing factors include the Mach number, the Knudsen number, the wall accommodation coefficient, and the rotation parameter of the cylinder.

John et al. [15,22] only considered the 2D planar flow over a rotating cylinder. On the other hand, the flow over a rotating sphere should be three-dimensional (3D) and may involve richer flow phenomena than its 2D counterpart. Additionally, the quantitative laws for the sphere and cylinder flows can also be different. In this paper, a 3D DSMC solver is used to simulate the air flow past a spinning sphere with a flight velocity of 2800 m/s and a flight altitude of 100 km. The formation of the inverse Magnus force is explained based

on the DSMC results. Additionally, the influences of the rotation rate on the flow field and aerodynamic characteristics are investigated. Such a study on the inverse Magnus effect will facilitate the understanding of the difference between rarefied and continuum flows. In engineering applications, the current study will also be useful for predicting the trajectory of space debris and exploring flight in the upper atmosphere with a high lift-to-drag ratio.

The remainder of this article is organized as follows. In Section 2, the numerical method and its validation are presented. Then, Section 3 describes the physical problems and the numerical treatments. The numerical results are discussed in detail in Section 4. For different rotation rates of the sphere, the 3D flow patterns, the surface quantities, and the aerodynamic forces are compared and analyzed. Finally, some conclusions are drawn in Section 5.

## 2. The Numerical Method

In this section, the numerical method used in this investigation is described, followed by two benchmark cases to validate the in-house code developed by the first author in previous works [23–25].

### 2.1. The Direct Simulation Monte Carlo Method

In the DSMC method, the objects of the simulation are samples of the real molecules that constitute the gas. By utilizing the Monte Carlo technique, the DSMC method can solve the gas-kinetic Boltzmann equation [26] in a probabilistic manner. In each DSMC time step, the free motions of molecules and the collisions between molecules are decoupled. First, the free motions of all molecules are tracked during the time step. Then, all binary collisions that should happen in this time step are performed. Such an algorithm can reproduce the physical process underlying the Boltzmann equation, as long as the time step is a fraction of the mean collision time of gas molecules. The macroscopic flow field can be obtained by sampling the microscopic quantities in each grid cell. Similarly, the aerodynamic force/heating distributions on the solid wall boundary can be derived from the statistics of microscopic fluxes.

The DSMC solver used in this investigation is based on the body-fitted grid and the corresponding particle tracking strategy, so that curved boundaries can be treated conveniently. The present DSMC solver can handle arbitrary geometries using multi-block structured or unstructured grids. The simulated gas can be a mixture of multiple species, and each species can be monatomic or polyatomic. The high-temperature gas effect is partially considered by simulating the vibrational excitation and the relaxation of internal energy modes. For collisions between gas molecules and the interaction between gas molecules and solid surfaces, there are different models to be selected.

In this paper, the no-time-counter (NTC) scheme [20] is employed to perform the pairwise collisions in each grid cell during one time step, so that the collision rates between molecules can be correct. The variable hard sphere (VHS) model [20] is adopted for the calculation of collision cross-sections and scattering angles. For the energy exchanges between translational/rotational/vibrational modes in inelastic collisions, the Larsen–Borgnakke redistribution approach [27] is used, and the relaxation rate of vibrational energy is consistent with the Millikan–White expression [28]. The Maxwellian model [20] describes the reflection of a gas molecule on the solid surface, where the probability of diffuse reflection is  $\alpha$  (called the accommodation coefficient), and the probability of specular reflection is  $1 - \alpha$ .

### 2.2. Code Validation

The first case corresponds to the experiment conducted by Holden et al. [29] using the low-density wind tunnel at Calspan-University of Buffalo Research Center (CUBRC). A nitrogen stream flows over a double-cone configuration at Mach 15.6, with a global Knudsen number of 0.00084. Interactions between shock waves, boundary layers, and the recirculation zone characterize this complex flow. In addition, the flow is vibrational

nonequilibrium and is also slightly influenced by rarefaction. More details about the geometric and flow conditions can be found in Ref. [30].

An axisymmetric DSMC simulation was performed, and the results of the flow patterns and quantities along the cone surface are shown in Figures 1 and 2. The positions of the separation and reattachment points coincide with the results reported by other researchers [31]. The DSMC predictions of the wall pressure and wall heat flux distributions also agree well with the experimental data [29], as shown in Figure 2.

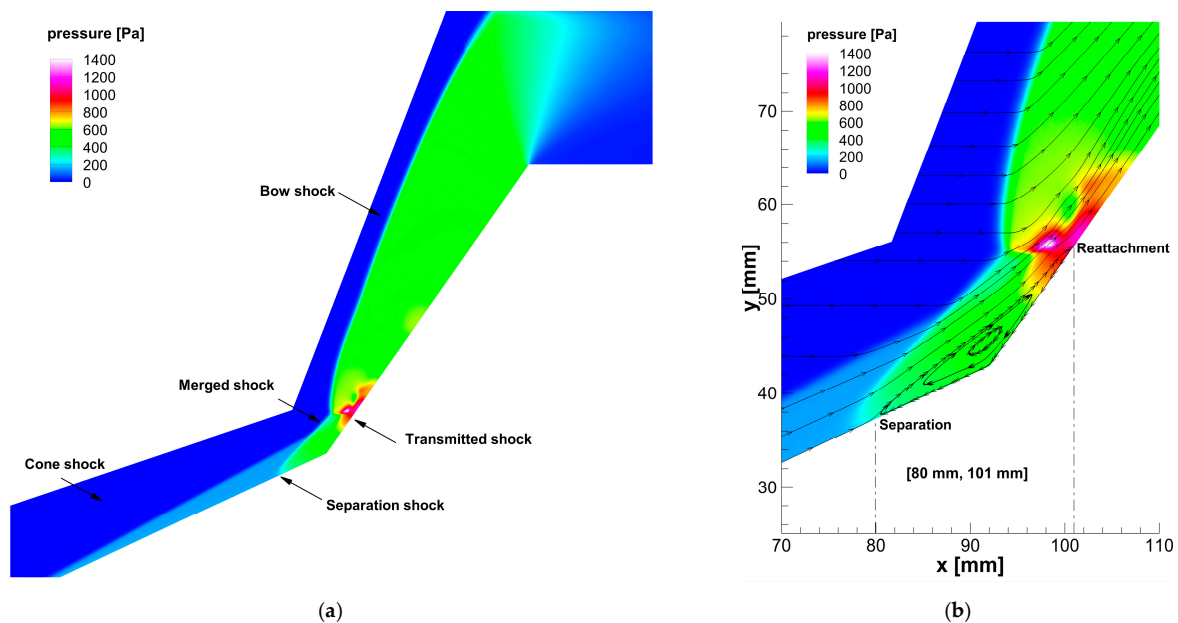


**Figure 1.** DSMC results of the hyperbolic flow over a double cone configuration: (a) pressure contours and the shock waves; (b) streamlines near the corner and the recirculation zone.

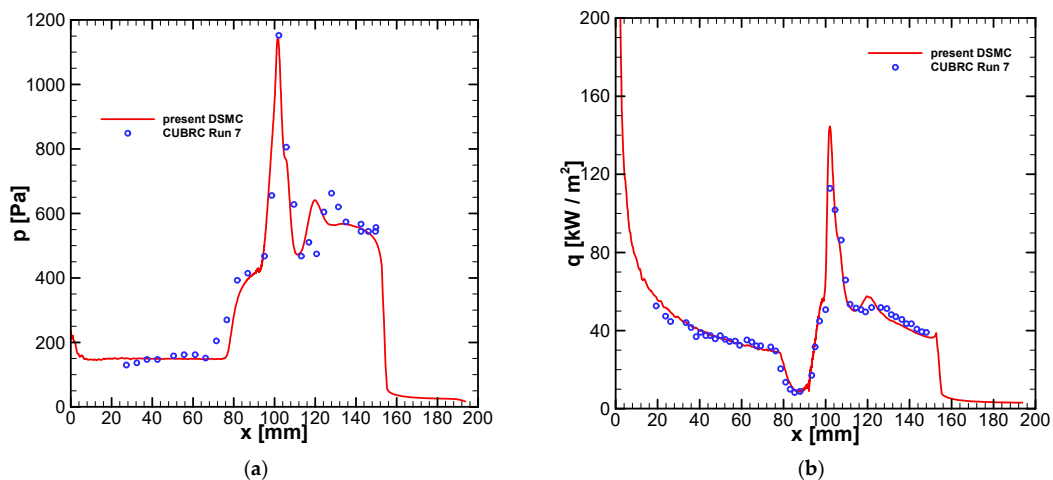


**Figure 2.** Comparison of the DSMC results and the experimental data [29] of the surface pressure and heat flux along the double-cone model: (a) distribution of pressure on the wall; (b) distribution of heat flux on the wall.

Another benchmark test is to reproduce the experimental results for the hypersonic nitrogen flow over a 70-degree blunt cone [32,33], which was studied in the SR3 wind tunnel. The working condition at a 10-degree angle of attack is considered and simulated using a 3D DSMC simulation. The freestream Mach number is about 20, but the total enthalpy of this flow is as low as 1 MJ/kg. Therefore, the chemical reaction can be ignored. The

Knudsen number based on the diameter is 0.034, indicating stronger rarefaction compared to the double-cone case.

The computational grid for half of the geometric model and the DSMC results are displayed in Figure 3. For the density field, a reasonable agreement can be reached between the DSMC simulation and the experiment [32]. The wall heat fluxes are also measured at several points on the cone in this experiment [33], and, as shown in Figure 4, the DSMC results match the experimental data well.

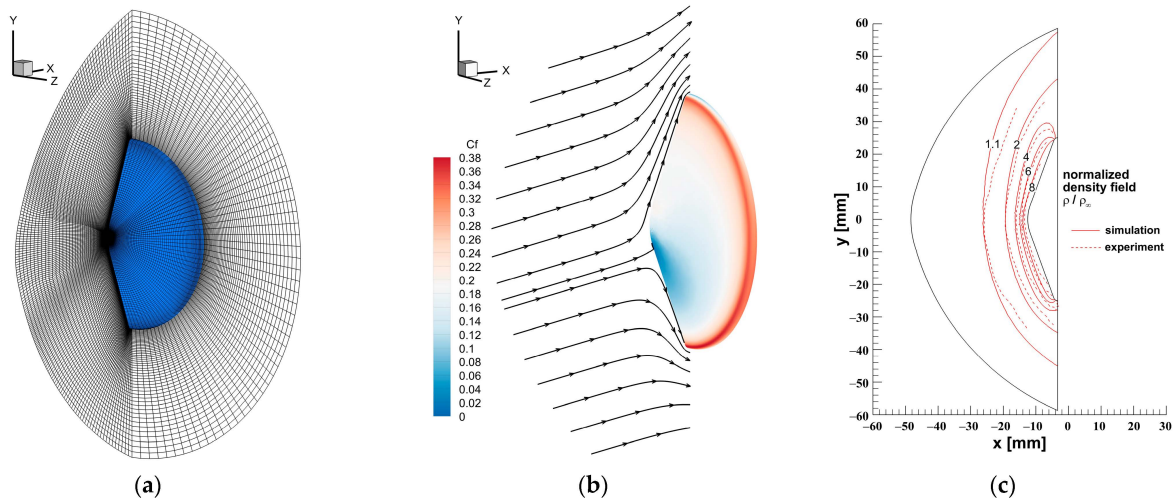


**Figure 3.** DSMC grid and results of the hypersonic rarefied flow over a blunt cone: (a) computational grid; (b) streamlines on the plane of symmetry and contour of skin friction coefficient over the cone surface; (c) contour lines of the normalized density in comparison with the experimental measurements [32].

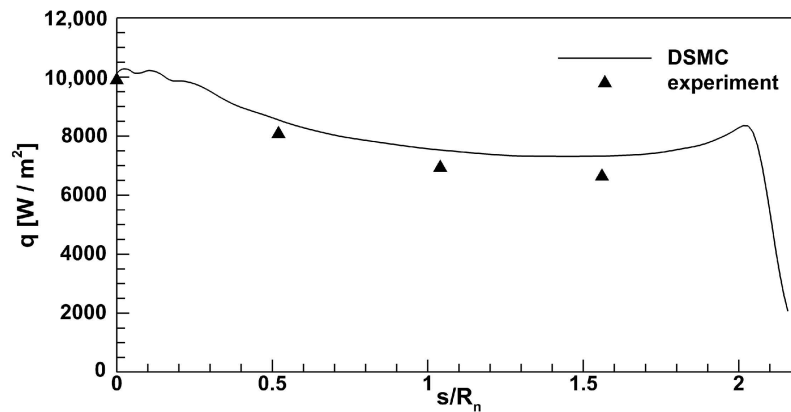


**Figure 4.** Comparison of the DSMC results for the heat flux distribution on the surface of a cone and the corresponding experimental results [33]. The horizontal axis is the normalized distance along the cone surface measured from the nose of the cone, where  $R_n$  denotes the nose radius.

### 3. Problem Description

This study concerns the hypersonic rarefied flows past a sphere rotating at different angular speeds. In this section, the geometric and flow parameters are tabulated in detail, followed by information about DSMC simulations for these flows.

#### 3.1. Flow Conditions

In all simulations, the working gas is air, which is approximately treated as a mixture of nitrogen and oxygen. The fractions of  $N_2$  molecules and  $O_2$  molecules are 78.8% and 21.2%, respectively. The velocity of the freestream is  $V_\infty = 2800$  m/s, and the thermodynamic parameters of the stream are similar to those of the atmosphere at the altitude of 100 km.

The sphere with a radius  $R = 0.1$  m (diameter  $D = 0.2$  m) is rotating at a constant angular velocity  $\omega$ . The axis of rotation is perpendicular to the freestream velocity. A dimensionless rotation parameter  $W$  is defined as the maximum linear velocity on the sphere to the magnitude of the freestream velocity, so  $W = \omega R / V_\infty$ . Five different values of  $\omega$  are considered here, and the corresponding values of the rotation parameter  $W$  are 0, 0.25, 0.50, 0.75, and 1.00. For  $W = 1.00$ ,  $\omega$  is 4456 revolutions per second. The wall is assumed to be isothermal at the temperature  $T_w = 300$  K, with full thermal accommodation  $\alpha = 1$ .

Important parameters are listed in Table 1. The freestream Mach number is 10. The Knudsen number here is the ratio of the freestream mean free path  $\lambda_\infty$  to the diameter  $D$ , and its value is 0.51, indicating a typical flow rarefaction in the transition regime.

**Table 1.** Conditions for the freestream and the wall in the study of the inverse Magnus effect.

Flow Conditions	Values
number density $n_\infty$	$1.189 \times 10^{19} \text{ m}^{-3}$
freestream velocity $V_\infty$	2800 m/s
freestream temperature $T_\infty$	195 K
wall temperature $T_w$	300 K
diameter of sphere $D$	0.2 m
accommodation coefficient $\alpha$	1
freestream Mach number $M_\infty$	10
Knudsen number $Kn_\infty$	0.51
rotation parameter $W$	0.00, 0.25, 0.50, 0.75, 1.00

### 3.2. Computational Settings and Parameters

Since there is a prescribed motion of the wall surface, the DSMC solver must incorporate the moving wall boundary condition. To be more specific, the linear velocity of a point on the sphere should be considered in two modules of the DSMC code: (1) the reflection of the gas molecules on the surface and (2) the sampling of incident and reflected momentum/energy for every surface element.

First, for the reflection model (e.g., diffuse reflection), its input and output variables should be regarded as the molecular velocities relative to the hitting point on the sphere. Therefore, the velocity of the post-reflection molecule should be calculated by

$$\mathbf{c} = \mathbf{V}_w + \mathbf{c}_{re} \quad (1)$$

where molecular velocity  $\mathbf{c}_{re}$  is the output of the reflection model, and  $\mathbf{V}_w$  is the velocity of the hitting point on the moving wall.

Another treatment for the moving wall is related to the sampling procedure for the calculation of surface pressure, friction, and heat flux. When sampling the incident and reflected momentum and energy, the molecular velocity relative to the wall (i.e.,  $\mathbf{c} - \mathbf{V}_w$ ) should be used.

The coordinate system, the computational domain, and the grid are demonstrated in Figure 5. The  $x$ -axis is aligned with the freestream velocity  $V_\infty$ , and the direction of the  $z$ -axis is the same as the angular velocity vector  $\omega$ . The origin of the coordinates is placed at the center of the sphere. Note that the flow is symmetric about the  $xy$  plane, and therefore only half of the space ( $z > 0$ ) needs to be considered. The computational domain is a hemisphere with a radius  $R_d = 7R$ . The body-fitted grid contains 108,000 hexahedral cells, and the minimum cell size is about 4 mm.

At the initial time, the flow field is assumed to be uniform and in equilibrium with the parameters of the freestream. A total of 10.8 million simulation particles are assigned to the grid cells, so there are 100 particles per cell after initialization. The time step size is set to  $\Delta t = 4 \times 10^{-6}$  s, and cumulative sampling starts from  $t = 4$  ms. It takes 20,000 flow-field samplings to obtain low-noise DSMC results for macroscopic quantities.

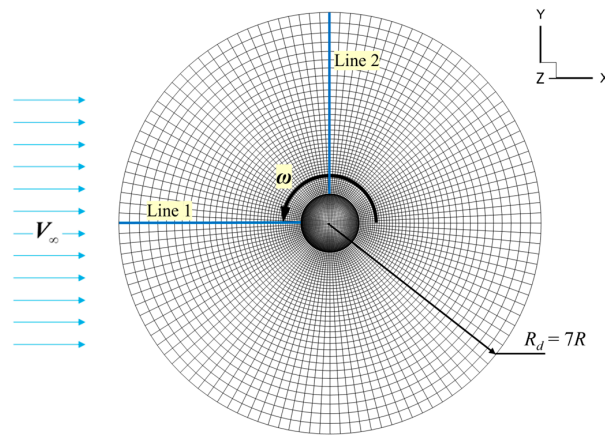


**Figure 5.** Coordinate system and the computational grid for the DSMC simulation of the hypersonic rarefied flow over a rotating sphere.

The above computational parameters for DSMC simulations are summarized in the second column of Table 2.

**Table 2.** DSMC parameters in the simulations of the rotating sphere flow problems.

Computational Parameters	Standard	Refined
number of cells	108,000	240,000
number of particles per cell	100	100
the minimum cell size	4 mm	2 mm
time step size	$4 \times 10^{-6}$ s	$2 \times 10^{-6}$ s

In order to verify that the DSMC results are independent of the grid and the time step, a refined grid and a reduced time step size (the last column in Table 2) are used to redo the DSMC simulation of the sphere flow under the condition of  $W = 0$ . Figure 6 compares the DSMC results using the standard and the refined grids. Flow variables along Line 1 and Line 2, marked in Figure 5, are extracted for comparison. The temperature profiles along Line 1 are plotted in Figure 6a, and the velocity profiles along Line 2 are shown in Figure 6b. The comparisons indicate that the DSMC simulations with different computational parameters yield almost indistinguishable solutions. Thus, in the remainder of this paper, the DSMC parameters all follow the standard settings.

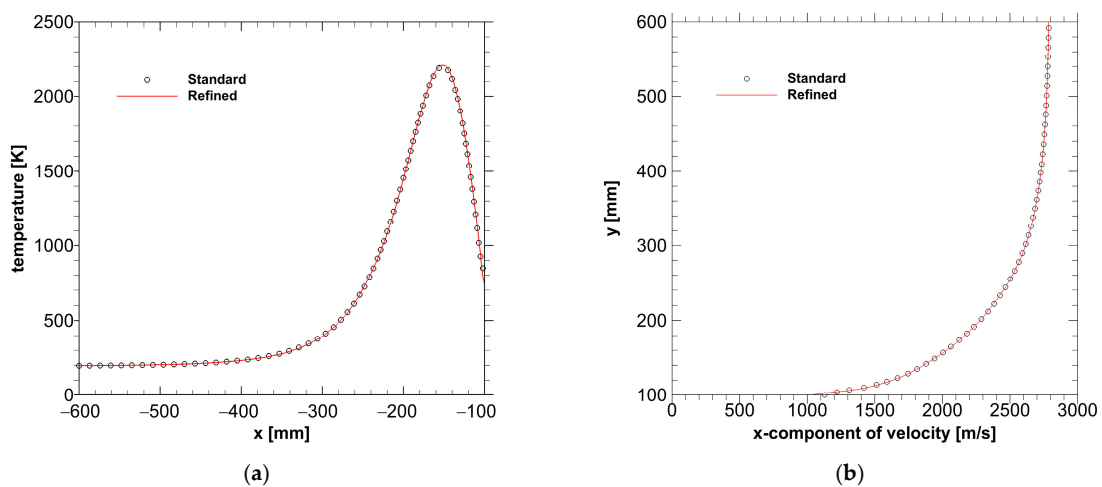


**Figure 6.** Comparison of the DSMC results of the flow described in Table 1 with parameter  $W = 0$ : (a) temperature profiles along Line 1 in Figure 5, computed with the standard and refined grids; (b) velocity profiles along Line 2 in Figure 5, computed with the standard and refined grids.

#### 4. Results and Discussion

The hypersonic rarefied flows past a rotating sphere, with different rotation parameters listed in Table 1, are simulated using the DSMC code validated in Section 2. The results of flow fields and aerodynamic characteristics are discussed in this Section.

##### 4.1. Flow Fields

The flow fields under conditions of  $W = 0.00, 0.25, 0.50, 0.75,$  and  $1.00$  are displayed in Figure 7a–e, respectively. Under the hypersonic rarefied flow conditions of  $M_\infty = 10$  and  $Kn_\infty = 0.51$  (or, equivalently, the Reynolds number  $Re_\infty = 22$ ), the flow features are distinct from their counterparts in the continuum flow regime. For all cases considered here, no flow separation is observed. Each flow field is highly diffusive, in which the shock wave and the boundary layer are substantially thickened and smeared, merging into one smooth zone around the sphere. No discontinuity exists in such a flow field, but the term “shock wave” is still used here to denote the front of the compression wave upstream of the sphere. In addition, there are remarkable velocity-slip phenomena on the wall surface, so the gas flow velocities on the sphere differ from the moving wall velocities.

Figure 7a shows the flow over a stationary sphere, and the flow field is symmetric about the  $x$ -axis. As the spinning rate increases, the asymmetry of the flow grows, and the following phenomena can be noticed. (1) As  $W$  increases, the disturbance from the rotating sphere propagates a longer distance upstream, and thus the disturbed area around the sphere is enlarged. (2) The rotation of the sphere distorts the shape of the shock wave and the shape of the compression zone ahead of the sphere. As  $W$  increases, the distortion becomes more severe. (3) The flow pattern on the sphere varies with  $W$ . On the windward side, the gas flow is significantly driven by the moving wall. On the leeward side, the gas streams along the meridional direction and is not affected by the wall motion because of the extremely low density of the gas and the weak interaction between the gas and the wall surface. (4) When  $W$  becomes large, a lateral streamline emerges prominently on the sphere. This lateral streamline emanates from the front stagnation point of the flow field. (5) As  $W$  increases, the front stagnation point shifts downstream (upward and rightward in the current view). Figure 7f shows the velocity profiles along the  $y$ -axis at different rotation rates. The amount of velocity slip at the wall ( $y = 100$  mm) becomes larger as  $W$  increases.

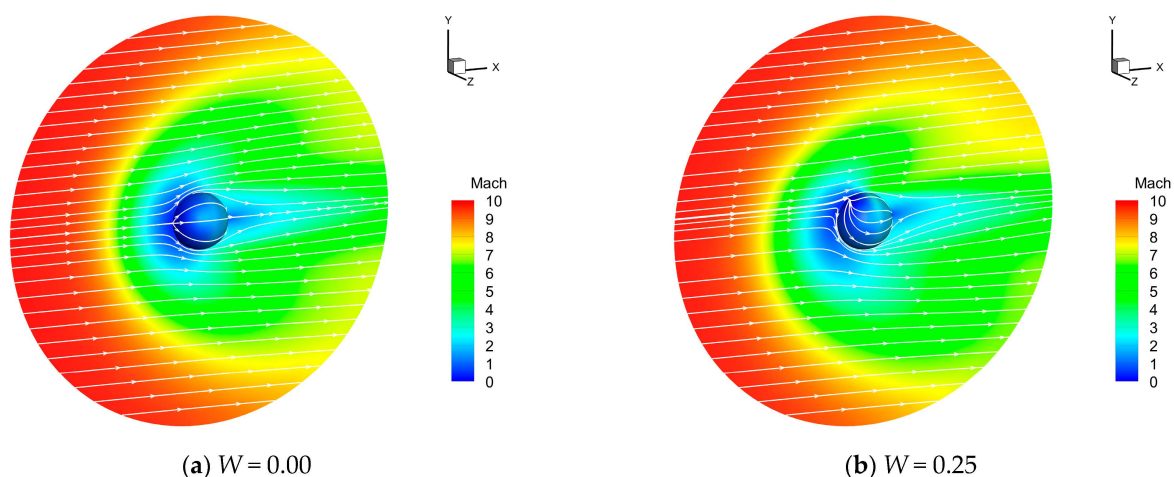
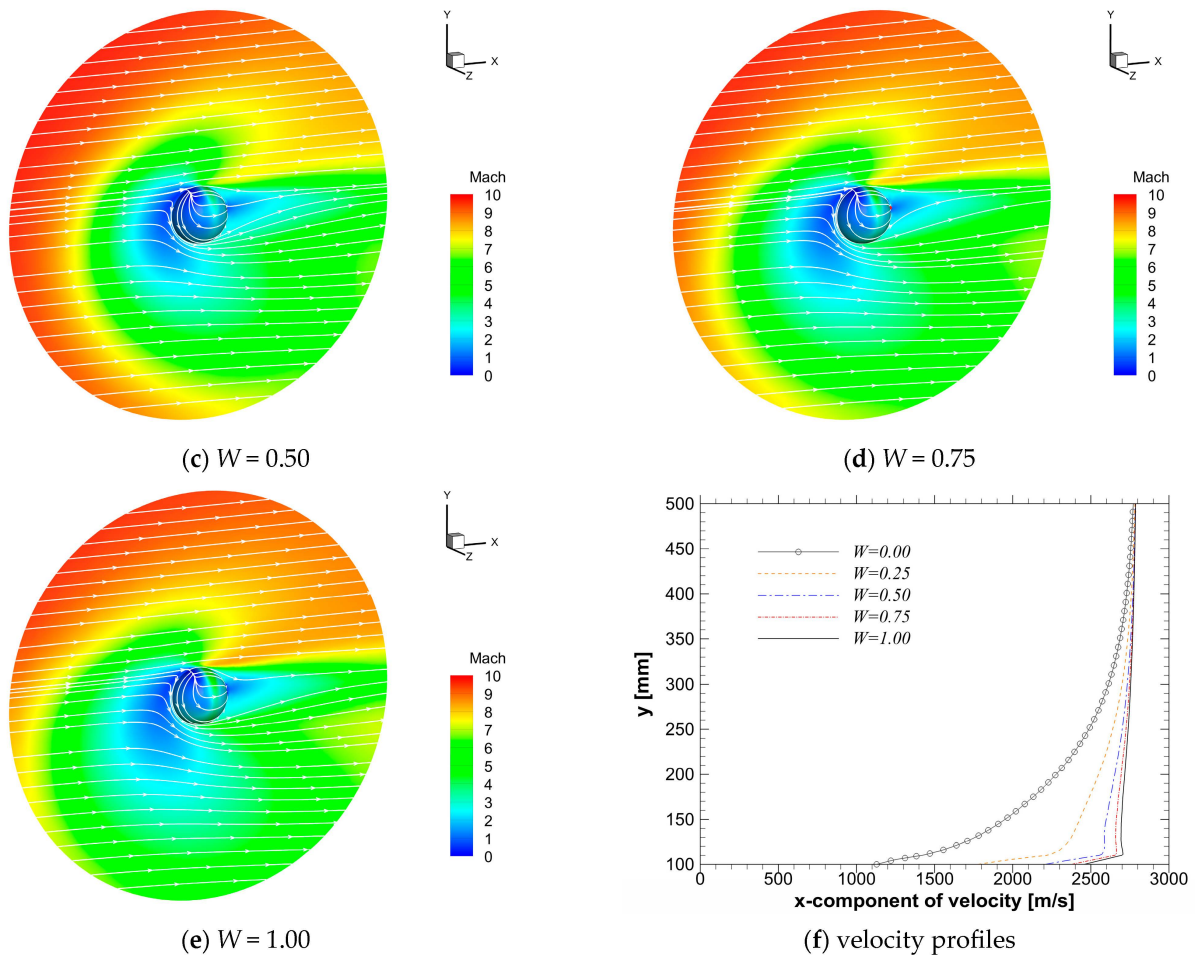


Figure 7. Cont.



**Figure 7.** The DSMC results for the flow fields for different rotation parameters  $W = \omega R/V_\infty$ . Subfigures (a–e) correspond to  $W = 0.00, 0.25, 0.50, 0.75,$  and  $1.00$ , respectively. The contour shows the distribution of the local Mach number on the symmetry plane and the sphere. Streamlines on the symmetry plane and the sphere are plotted. Subfigure (f): velocity profiles along Line 2 in Figure 5.

#### 4.2. Surface Quantities

This subsection is devoted to the presentation and analysis of the distributions of skin friction  $\tau_w(x_w)$ , pressure  $p_w(x_w)$ , and heat flux  $q_w(x_w)$  on the sphere. These quantities are expressed in terms of dimensionless coefficients:

$$C_f = \frac{|\tau_w|}{\rho_\infty V_\infty^2 / 2}, \quad C_p = \frac{p_w - p_\infty}{\rho_\infty V_\infty^2 / 2}, \quad C_h = \frac{q_w}{\rho_\infty V_\infty^3 / 2}, \quad (2)$$

where  $\rho_\infty$  and  $p_\infty$  are the freestream density and pressure, respectively. The influences of the rotation parameter on the distributions of surface quantities are discussed. Explanations are provided for how  $\tau_w(x_w)$  and  $p_w(x_w)$  contribute to the formation of the inverse Magnus force.

##### 4.2.1. Distribution of Wall Friction

When the sphere is at rest (Figure 8a), the distribution of the shear stress vector on the sphere is axisymmetric. As the rotation speed increases (Figure 8b–e), the symmetry is broken significantly, and the strength of skin friction is enhanced. The point of  $C_f = 0$  departs the leftmost pole on the sphere and moves toward the bottom. The region with a large magnitude of  $C_f$  is mainly the upper half of the windward side, where the directions of shear stresses are basically upward. The resultant force of these shear stresses becomes a lift  $F_y$  exerted on the sphere, directed toward the positive  $y$ -axis.

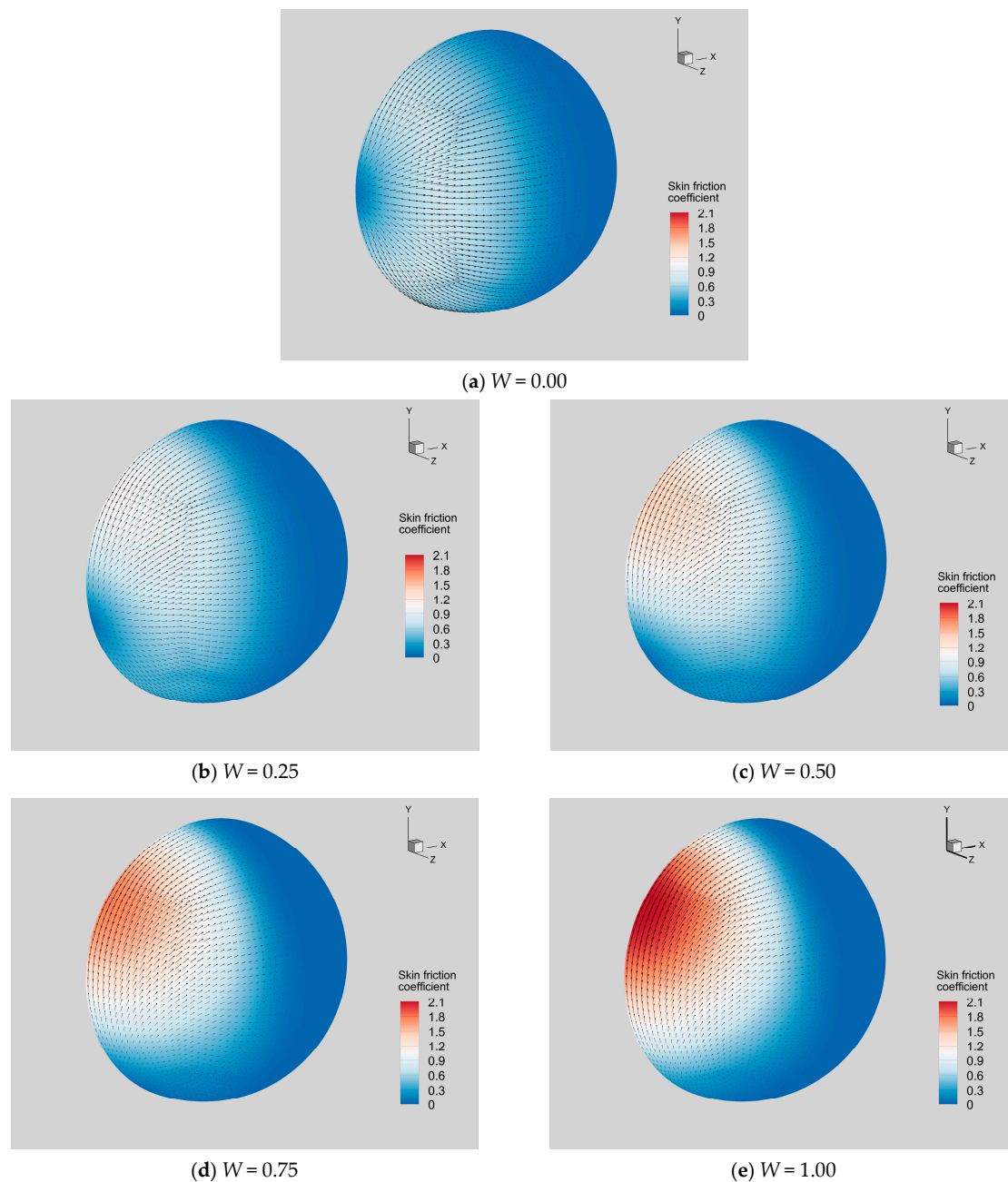


**Figure 8.** The DSMC results of the wall friction for different rotation parameters  $W = \omega R/V_\infty$ . Subfigures (a–e) correspond to  $W = 0.00, 0.25, 0.50, 0.75,$  and  $1.00$ , respectively. The contour shows the magnitude of  $C_f$ . The vectors show the directions of shear stresses.

These findings can be explained by comparing the distribution of shear stress with the field of relative velocity on the sphere. In Figure 9a, the magnitudes and directions of the wall shear stresses under the condition of  $W = 0.5$  are demonstrated. In Figure 9b, the relative velocity is the difference between the absolute gas velocity shown in Figure 7c and the linear velocity of the rotating wall surface. It can be observed that the direction of wall friction coincides with the direction of gas motion relative to the spinning sphere. The point at which  $C_f = 0$  is just the point where the gas velocity equals the wall velocity. According to the gas-kinetic interpretation of wall shear stress, the magnitude of  $\tau_w(x_w)$  is determined by the combining effects of the incident mass flux on the wall and the magnitude of relative velocity. The incident mass flux is large only on the windward side, while the relative velocity is large only on the top of sphere. As a result, strong friction is concentrated on the

upper half of the windward side, where the tangential momentum transfer between the gas molecules and the wall surface is rapid and effective.

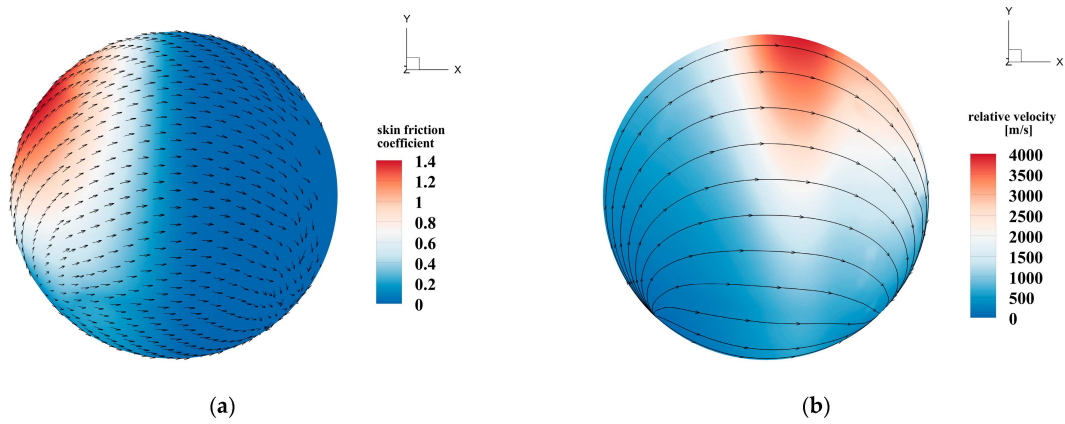


**Figure 9.** Relation between (a) the skin friction distribution and (b) the relative velocity field on the sphere with rotation parameter  $W = 0.5$ .

4.2.2. Distribution of Wall Pressure

Figure 10 demonstrates the contours of  $C_p$  on the sphere. For the stationary sphere (Figure 10a), the distribution of wall pressure is axisymmetric. The high pressure is concentrated on the windward side, with the maximum pressure appearing at the leftmost pole of the sphere. The variation of pressure distribution with the rotation parameter is shown in Figure 10b–e. The distribution of wall pressure remains symmetric when the sphere rotates, in contrast to the velocity field shown in Figure 7. As  $W$  increases, the position of the maximum pressure stays unchanged, but the magnitude of  $C_p$  declines slightly.

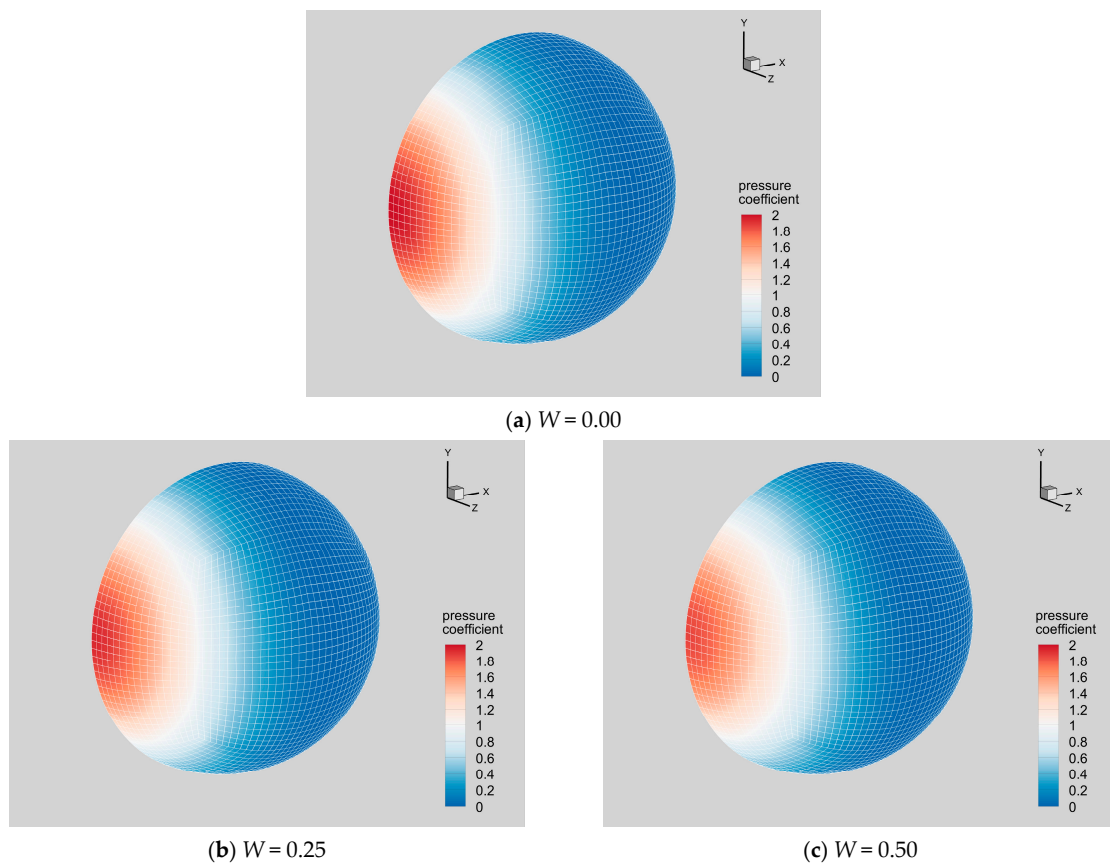


**Figure 10.** Cont.

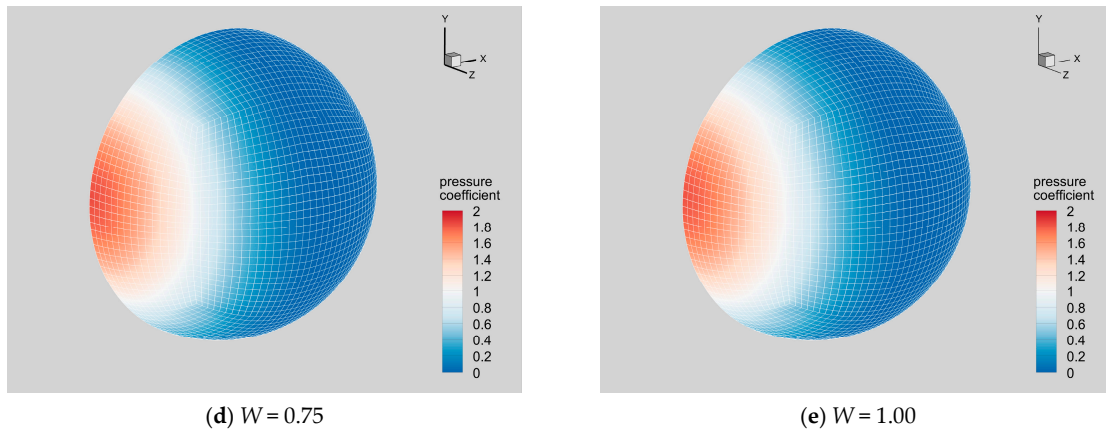


**Figure 10.** The DSMC results of pressure coefficient  $C_p$  on the sphere for different rotation parameters  $W = \omega R/V_\infty$ . Subfigures (a–e) correspond to  $W = 0.00, 0.25, 0.50, 0.75,$  and  $1.00$ , respectively.

The wall pressure distribution makes a major contribution to the aerodynamic drag  $F_x$ , but makes little contribution to the lift  $F_y$  (the inverse Magnus force). The roles of pressure distribution in the formation of lift are entirely different between rarefied flow and continuum flow.

#### 4.2.3. Distribution of Wall Heat Flux

Figure 11 provides the aerodynamic heating results for different rotation parameters. When  $W = 0$ , the heat flux distributes symmetrically about the  $x$ -axis, with  $C_{h,max} = 0.8$  at the leftmost pole of the sphere. As the rotation speed increases, the high-heat-flux region moves upward and  $C_{h,max}$  sharply grows to 2.1 when  $W = 1$ . The reason for this strong heat transfer is the high energy in the relative motion between the incident molecules and the fast-moving surface. For similar reasons, presented in Section 4.2.1, the intense heat transfer is concentrated on the upper half of the windward side of the sphere.

#### 4.3. Overall Aerodynamic Characteristics

Based on the DSMC data for wall pressure and shear stress, integrations over the sphere yield the drag  $F_x$ , the lift  $F_y$ , and the moment about the  $z$ -axis  $M_z$ . These aerodynamic forces and moments are expressed in terms of dimensionless coefficients:

$$C_D = \frac{F_x}{(\rho_\infty V_\infty^2/2)(\pi R^2)}, \quad C_L = \frac{F_y}{(\rho_\infty V_\infty^2/2)(\pi R^2)}, \quad C_M = \frac{|M_z|}{(\rho_\infty V_\infty^2/2)(\pi R^2)R}. \quad (3)$$

For the hypersonic rarefied flow over a rotating sphere, the coefficients  $C_D, C_L,$  and  $C_M$  generally depend on the Mach number  $M_\infty$ , the Knudsen number  $Kn_\infty$ , the accommodation coefficient  $\alpha$ , the temperature ratio  $T_w/T_\infty$ , and the rotation parameter  $W$ . The present numerical investigation only concerns the effect of rotation on the aerodynamic characteristics, so other influencing factors are fixed. The DSMC results of  $C_D, C_L,$  and  $C_M$  are plotted as functions of  $W$ , and the corresponding theoretical free-molecular solutions are also presented for qualitative reference.

##### 4.3.1. Drag

In the free-molecular limit ( $Kn_\infty \rightarrow \infty$ ), an exact analytical solution can be derived for the rotating sphere flow problem, and the drag coefficient [18] reads

$$C_D = \frac{4S^4 + 4S^2 - 1}{2S^4} \text{erf}(S) + \frac{2S^2 + 1}{\sqrt{\pi}S^3} \exp(-S^2) + \frac{2\alpha\sqrt{\pi}}{3S} \sqrt{\frac{T_w}{T_\infty}} \quad (4)$$

where  $S$  is the freestream speed ratio, which differs from  $M_\infty$  only by a constant factor

$$S = \sqrt{\frac{\gamma}{2}} M_\infty \tag{5}$$

and  $\gamma = 1.4$  is the specific heat ratio of the freestream air. Under the flow conditions in this study, the free-molecular solution (4) becomes  $C_D = 2.2036$ , which is independent of  $W$ .

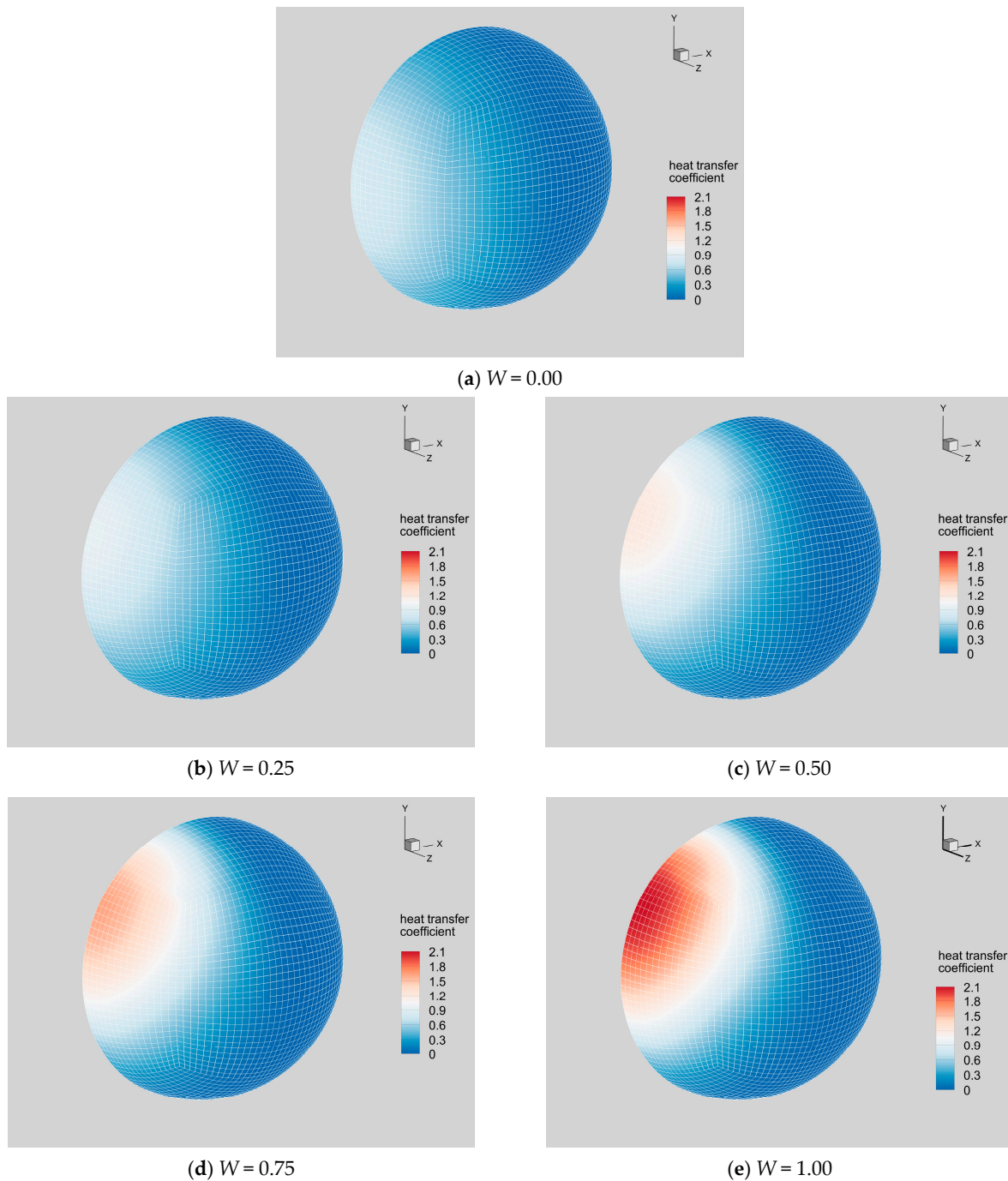


**Figure 11.** The DSMC results for the heat transfer coefficient  $C_h$  on the sphere for different rotation parameters  $W = \omega R/V_\infty$ . Subfigures (a–e) correspond to  $W = 0.00, 0.25, 0.50, 0.75,$  and  $1.00$ , respectively.

Figure 12 shows the drag coefficients computed through the DSMC method for different values of  $W$ , along with the theoretical solution under the free-molecular assumption. In comparison with the free-molecular solution, the simulation data are lower. This discrepancy is reasonable, because the flow Knudsen number  $Kn_\infty$  considered in this paper is only 0.51, while the commonly-used criteria for the free-molecular regime is  $Kn_\infty > 10$ . However, the variation tendency of  $C_D$  with the growth of  $W$  is similar to the free-molecular solution. As  $W$  increases, the drag of the sphere stays almost constant.

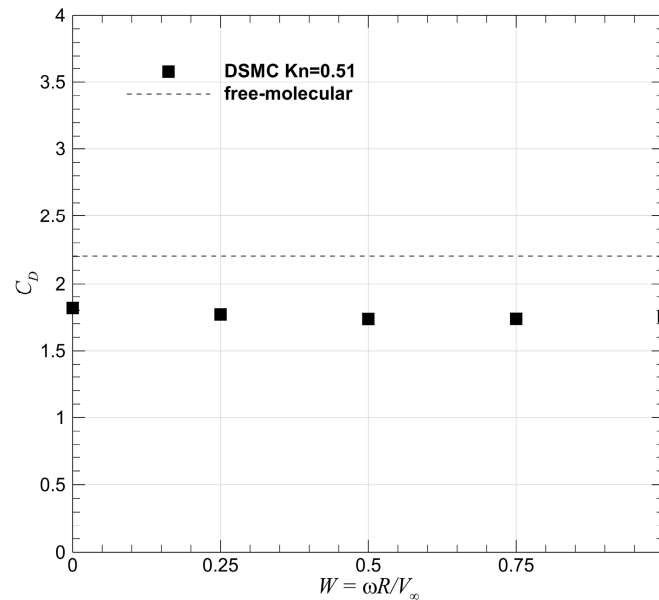


Figure 12. Drag coefficients of the sphere at different rotation parameters. Symbols: DSMC results; line: free-molecular solution.

#### 4.3.2. Lift

The free-molecular solution for the lift acting on the rotating sphere in hypersonic rarefied flows [18] has a simple form:

$$C_L = \frac{4\alpha}{3}W, \tag{6}$$

which indicates that  $C_L$  increases in proportion to  $W$ . Figure 13 displays the  $C_L$ - $W$  plots for both the free-molecular and the DSMC solutions. At  $Kn_\infty = 0.51$ , the relation between the lift and the rotation speed is qualitatively similar to that in Equation (6), but the slope is smaller than  $4\alpha/3$ . Again, this is because the rarefaction of the simulated flow is not strong enough to satisfy the free-molecular assumption underlying Equation (6).

The positivity of the lift  $F_y$  means that it has an upward direction, which is the same as  $\omega \times V_\infty$  and opposite to the direction inferred from the knowledge of the conventional Magnus effect in low-speed continuum flows. By utilizing the rotation, a linearly increasing lift can be gained without any increase in drag. Thus, the lift-to-drag ratio of the sphere can be effectively elevated in this manner.

#### 4.3.3. Moment

To the best knowledge of the authors, the formula for the aerodynamic moment acting on the rotating sphere in the free-molecular regime has not been reported in the literature. Following the procedures to derive the formulas of  $C_D$  and  $C_L$ , we obtain the free-molecular solution for the moment coefficient  $C_M$ :

$$C_M = \frac{2\alpha W}{\pi} \left\{ \frac{1}{\sqrt{\pi}S} \int_0^\pi \int_0^\pi \sin^3 \varphi \exp[-(S \sin \varphi \cos \theta)^2] d\theta d\varphi + \int_0^\pi \int_0^\pi \sin^4 \varphi \cos \theta \operatorname{erf}(S \sin \varphi \cos \theta) d\theta d\varphi \right\} \tag{7}$$

where  $\varphi$  and  $\theta$  are the angular parameters on the sphere. Note that, at this moment,  $M$  is with respect to the sphere center, and it is toward the negative  $z$ -direction, which is just opposite to the direction of  $\omega$ . Equation (7) indicates the linear dependence of the aerodynamic moment on the rotation speed.

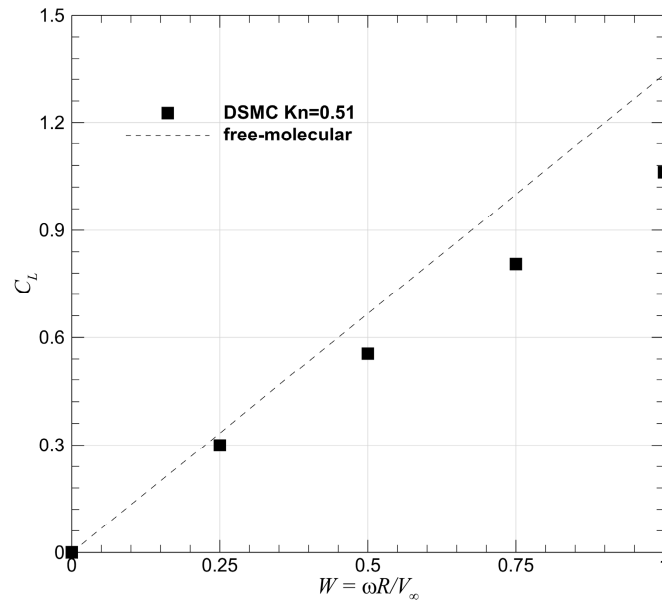


**Figure 13.** Lift coefficients of the sphere at different rotation parameters. Symbols: DSMC results; line: free-molecular solution.

Figure 14 shows the DSMC results of  $C_M$  at different rotation parameters, along with the theoretical solution in the free-molecular limit for reference. The DSMC results at  $Kn_\infty = 0.51$  are qualitatively consistent with the free-molecular formula, but the medium rarefaction considered in the simulation makes the DSMC results smaller than the free-molecular predictions.

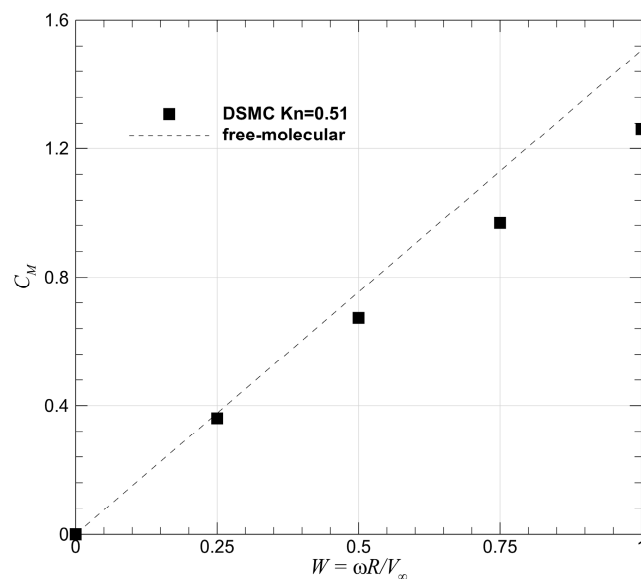


**Figure 14.** Moment coefficients of the sphere at different rotation parameters. Symbols: DSMC results; line: free-molecular solution.

### 5. Conclusions

An in-house DSMC solver is validated and extended to incorporate the moving wall boundary condition. A series of 3D DSMC simulations were carried out to study

the hypersonic rarefied flow past a rotating sphere. Flow phenomena and aerodynamic characteristics under the conditions of  $M_\infty = 10$ ,  $Kn_\infty = 0.51$ ,  $\alpha = 1$ , and  $T_w/T_\infty = 0.65$  are discussed in detail, with conclusions as follows:

- (1) A lift, called the inverse Magnus force, is exerted on the rotating sphere. Its direction is opposite to that observed in the Magnus effect for continuum flows.
- (2) The rotation of the sphere leads to a distortion of the shock wave, an increase in the shock stand-off distance, and changes to other flow features, e.g., the position of the front stagnation point.
- (3) Velocity slip is very significant on the wall surface, and fascinating flow patterns can be formed on the sphere under different rotation rates.
- (4) The symmetry of the wall pressure distribution is not affected by the rotation of the sphere, and thus the pressure distribution makes no contribution to the formation of the inverse Magnus force.
- (5) The formation of the inverse Magnus force is attributed to skin friction, which is caused by the relative motion between the gas and the wall surface. The strong-friction region is on the upper half of the sphere's windward side.
- (6) The microscopic mechanism of the inverse Magnus effect is the transfer of tangential momentum from the incident gas molecules to the windward surface of the rotating sphere.
- (7) As the rotation rate increases, the lift and the moment on the sphere increase in proportion to the rotation rate, while the drag remains almost unchanged. In addition, the aerodynamic heating on the sphere is greatly enhanced with the increase in rotation rate.

Future work includes extending the current DSMC database for more comprehensive investigations of the inverse Magnus effect. Parametric studies for key flow conditions (e.g.,  $M_\infty$  and  $Kn_\infty$ ) are necessary to reveal their influences on the inverse Magnus effect.

**Author Contributions:** Conceptualization, Y.J.; methodology, Y.J.; software, Y.J. and Y.L.; validation, Y.J., Y.L. and S.Z.; formal analysis, Y.J. and Y.L.; investigation, Y.J., Y.L. and S.Z.; resources, Y.J.; data curation, Y.J. and Y.L.; writing—original draft preparation, Y.J. and S.Z.; writing—review and editing, Y.J.; visualization, Y.J. and Y.L.; supervision, Y.J.; project administration, Y.J.; funding acquisition, Y.J. All authors have read and agreed to the published version of the manuscript.

**Funding:** This research was funded by the National Natural Science Foundation of China, grant number 12302388, and the National Innovation and Entrepreneurship Training Program for College Students, grant number S202310497203.

**Institutional Review Board Statement:** Not applicable.

**Informed Consent Statement:** Not applicable.

**Data Availability Statement:** The raw data supporting the conclusions of this article will be available by the authors on request.

**Acknowledgments:** The authors acknowledge Pengbo Yang for his efforts in visualizing the numerical data.

**Conflicts of Interest:** The authors declare no conflict of interest.

## References

1. Candler, G.V. Rate effects in hypersonic flows. *Annu. Rev. Fluid. Mech.* **2019**, *51*, 379–402. [[CrossRef](#)]
2. Cao, S.; Hao, J.; Klioutchnikov, I.; Wen, C.-Y.; Olivier, H.; Heufer, K.A. Transition to turbulence in hypersonic flow over a compression ramp due to intrinsic instability. *J. Fluid. Mech.* **2022**, *941*, A8. [[CrossRef](#)]
3. Guo, P.; Hao, J.; Wen, C.-Y. Interaction and breakdown induced by multiple optimal disturbances in hypersonic boundary layer. *J. Fluid. Mech.* **2023**, *974*, A50. [[CrossRef](#)]
4. Hao, J. On the low-frequency unsteadiness in shock wave–turbulent boundary layer interactions. *J. Fluid. Mech.* **2023**, *971*, A28. [[CrossRef](#)]
5. Liu, Q.; Baccarella, D.; Lee, T. Review of combustion stabilization for hypersonic airbreathing propulsion. *Prog. Aerosp. Sci.* **2020**, *119*, 100636. [[CrossRef](#)]
6. Ivanov, M.S.; Gimelshein, S.F. Computational hypersonic rarefied flows. *Annu. Rev. Fluid. Mech.* **1998**, *30*, 469–505. [[CrossRef](#)]

7. Schouler, M.; Preveraud, Y.; Mieussens, L. Survey of flight and numerical data of hypersonic rarefied flows encountered in earth orbit and atmospheric reentry. *Prog. Aerosp. Sci.* **2020**, *118*, 100638. [[CrossRef](#)]
8. Keerthi, A.; Geim, A.K.; Janardanan, A.; Rooney, A.P.; Esfandiari, A.; Hu, S.; Dar, S.A.; Grigorieva, I.V.; Haigh, S.J.; Wang, F.C.; et al. Ballistic molecular transport through two-dimensional channels. *Nature* **2018**, *558*, 420–424. [[CrossRef](#)]
9. Pfeiffer, M.; Beyer, J.; Vaubailon, J.; Matlovič, P.; Tóth, J.; Fasoulas, S.; Löhle, S. Numerical simulation of an iron meteoroid entering into Earth's atmosphere using DSMC and a radiation solver with comparison to ground testing data. *Icarus* **2024**, *407*, 115768. [[CrossRef](#)]
10. Cardona, V.; Jousot, R.; Lago, V. Shock/shock interferences in a supersonic rarefied flow: Experimental investigation. *Exp. Fluids* **2021**, *62*, 135. [[CrossRef](#)]
11. Schwartzentruber, T.E.; Boyd, I.D. Progress and future prospects for particle-based simulation of hypersonic flow. *Prog. Aerosp. Sci.* **2015**, *72*, 66–79. [[CrossRef](#)]
12. Swanson, W.M. The Magnus effect: A summary of investigations to date. *J. Basic. Eng.* **1961**, *83*, 461–470. [[CrossRef](#)]
13. Seifert, J. A review of the Magnus effect in aeronautics. *Prog. Aerosp. Sci.* **2012**, *55*, 17–45. [[CrossRef](#)]
14. Weidman, P.D.; Herczynski, A. On the inverse Magnus effect in free molecular flow. *Phys. Fluids* **2004**, *16*, 9–12. [[CrossRef](#)]
15. John, B.; Gu, X.-J.; Barber, R.W.; Emerson, D.R. High-speed rarefied flow past a rotating cylinder: The inverse Magnus effect. *AIAA J.* **2016**, *54*, 1670–1681. [[CrossRef](#)]
16. Shen, Q.; Huang, F.; Cheng, X.-L.; Jin, X.-H. On characteristics of upper atmosphere aerodynamics of flying vehicles. *Phys. Gases* **2021**, *6*, 1–9.
17. Anderson, J.D. *Fundamentals of Aerodynamics*, 5th ed.; McGraw-Hill: New York, NY, USA, 2011; pp. 274–280.
18. Wang, C.-T. Free molecular flow over a rotating sphere. *AIAA J.* **1972**, *10*, 713–714. [[CrossRef](#)]
19. Borg, K.I.; Soderholm, L.H.; Essen, H. Force on a spinning sphere moving in a rarefied gas. *Phys. Fluids* **2003**, *15*, 736–741. [[CrossRef](#)]
20. Bird, G.A. *Molecular Gas Dynamics and the Direct Simulation of Gas Flows*, 2nd ed.; Clarendon Press: Oxford, UK, 1994.
21. Boyd, I.D. Computation of hypersonic flows using the direct simulation Monte Carlo method. *J. Spacecr. Rocket.* **2015**, *52*, 38–53. [[CrossRef](#)]
22. John, B.; Gu, X.-J.; Emerson, D.R. Computation of aerodynamic forces under nonequilibrium conditions: Flow past a spinning cylinder. *AIAA J.* **2018**, *56*, 4219–4224. [[CrossRef](#)]
23. Jiang, Y.; Gao, Z.; Jiang, C.; Lee, C.-H. Hypersonic aeroheating characteristics of leading edges with different nose radii. *J. Thermophys. Heat. Transf.* **2017**, *31*, 538–548. [[CrossRef](#)]
24. Wang, J.; Chen, L.; Jiang, Y.; Lee, C.-H. Particle simulation of an anode-layer Hall thruster plume using an anisotropic scattering model. *Acta Astronaut.* **2020**, *175*, 19–31. [[CrossRef](#)]
25. Liu, W.; Zhang, J.; Jiang, Y.; Chen, L.; Lee, C.-H. DSMC study of hypersonic rarefied flow using the Cercignani–Lampis–Lord model and a molecular-dynamics-based scattering database. *Phys. Fluids* **2021**, *33*, 072003. [[CrossRef](#)]
26. Kremer, G.M. *An Introduction to the Boltzmann Equation and Transport Processes in Gases*, 1st ed.; Springer: Berlin, Germany, 2010.
27. Borgnakke, C.; Larsen, P.S. Statistical collision model for Monte Carlo simulation of polyatomic gas mixture. *J. Comput. Phys.* **1975**, *18*, 405–420. [[CrossRef](#)]
28. Millikan, R.C.; White, D.R. Systematics of vibrational relaxation. *J. Chem. Phys.* **1963**, *39*, 3209–3213. [[CrossRef](#)]
29. Holden, M.S.; Wadhams, T.P. A database of aerothermal measurements in hypersonic flow in “building block” experiments for CFD validation. In Proceedings of the 41st AIAA Aerospace Sciences Meeting and Exhibit, Reno, NV, USA, 6–9 January 2003.
30. Moss, J.N.; Bird, G.A. Direct simulation Monte Carlo simulations of hypersonic flows with shock interactions. *AIAA J.* **2005**, *43*, 2565–2573. [[CrossRef](#)]
31. Bird, G.A. *The DSMC Method*, 1st ed.; CreateSpace Independent Publishing Platform: San Bernardino, CA, USA, 2013.
32. Allègre, J.; Bisch, D.; Lengrand, J.C. Experimental rarefied density flowfield at hypersonic conditions over 70-degree blunted cone. *J. Spacecr. Rocket.* **1997**, *34*, 714–718. [[CrossRef](#)]
33. Allègre, J.; Bisch, D.; Lengrand, J.C. Experimental rarefied heat transfer at hypersonic conditions over 70-degree blunted cone. *J. Spacecr. Rocket.* **1997**, *34*, 724–728. [[CrossRef](#)]

**Disclaimer/Publisher's Note:** The statements, opinions and data contained in all publications are solely those of the individual author(s) and contributor(s) and not of MDPI and/or the editor(s). MDPI and/or the editor(s) disclaim responsibility for any injury to people or property resulting from any ideas, methods, instructions or products referred to in the content.